Research Article

pISSN 2799-8525 · eISSN 2799-8681
J Powder Mater 2025;32(4):288-298

Journal of
Powder Materials

Cost-effective Fabrication of Near β-Ti Alloy via L-PBF: Process Optimization of In-Situ Alloying Ti-3Fe

Sehun Kim, Ukju Gim, Taehu Kang, Jongik Lee, Sanghee Jeong, Jimin Han, Bin Lee*

Department of Advanced Materials Engineering Kyung Hee University, Yongin 17104, Republic of Korea

This study presents a cost-effective approach to fabricating near β-Ti alloys via in-situ alloying during laser powder bed fusion (L-PBF). A blend of non-spherical pure Ti, 3 wt.% Fe, and 0.1 wt.% SiO_2 nanoparticles was used to induce β-phase stabilization and improve flowability. Twenty-five process conditions were evaluated across a volumetric energy density range of 31.75-214.30 J/mm^3, achieving a maximum relative density of 99.21% at 89.29 J/mm^3. X-ray diffraction analysis revealed that the β-Ti phase was partially retained at room temperature, accompanied by lattice contraction in the α′-Ti structure, indicating successful Fe incorporation. Elemental mapping confirmed that the Fe distribution was homogeneous, without significant segregation. Compared to pure Ti, the Ti-3Fe sample exhibited a 49.2% increase in Vickers hardness and notable improvements in yield and ultimate tensile strengths. These results demonstrate the feasibility of in-situ alloying with low-cost elemental powders to produce high-performance near β-Ti alloys using L-PBF.

Keywords: Laser powder bed fusion; β-Ti alloy; Flowability; In-situ alloying; Mechanical properties

Received: July 10, 2025
Revised: August 11, 2025
Accepted: August 11, 2025

***Corresponding author:**
Bin Lee
E-mail: leebin@khu.ac.kr

1. Introduction

Titanium (Ti) and its alloys are widely employed in various sectors, including aerospace, biomedical fields, and mobility, due to their high specific strength, exceptional corrosion resistance, and superior biocompatibility [1, 2]. Ti is an allotropic metal, exhibiting two primary equilibrium phases: the α phase, which exhibits a hexagonal close-packed (HCP) structure at lower temperatures, and the β phase, which exhibits a body-centered cubic (BCC) structure at higher temperatures. The mechanical properties of Ti alloys are influenced by the ratio of alloying elements incorporated to stabilization of each phase [3, 4]. Ti alloys are typically classified as α-Ti, α+β-Ti, or β-Ti alloys based on the phase stability at room temperature. The β-Ti alloys investigated in this study are characterized by improved processability and biocompatibility due to the stabilization of the β phase. These alloys are further classified as near β, metastable β, or stable β Ti alloys, depending on the content of elements that stabilize the β phase.

The molybdenum equivalent (Mo_{eq}) formula, as defined in equation (1), is employed to categorize β-Ti alloys.

$$\begin{aligned} Mo_{eq} = {} & 1.0(\text{wt.\% Mo}) + 0.67(\text{wt.\% V}) \\ & + 0.44(\text{wt.\% W}) + 0.28(\text{wt.\% Nb}) + 0.22(\text{wt.\% Ta}) \\ & + 2.9(\text{wt.\% Fe}) + 1.6(\text{wt.\% Cr}) + 1.25(\text{wt.\% Ni}) \\ & + 1.70(\text{wt.\% Mn}) + 1.70(\text{wt.\% Co}) - 1.0(\text{wt.\% Al}) \end{aligned} \tag{1}$$

This formula provides a numerical measure that quantifies the degree of stabilization of the β phase, based on the addition of molybdenum (Mo), a well-known β-stabilizer. A higher Mo_{eq} value signifies enhanced β phase stability. According to this value, β-Ti alloys can be classified as detailed in Table 1 [5]. For instance, in this investigation, the incorporation of iron (Fe), a β phase stabilizing element, at a concentration of 3 wt.% yields an Mo_{eq} value of approximately 8.7, resulting in the formation of a near β-Ti alloy. This near β-Ti alloy is characterized by a microstructure wherein the α phase is distributed within the β matrix, thereby improving the alloy's strength and lowering the β-transus temperature, which confers advantages in hot forging

---

https://doi.org/10.4150/jpm.2025.00213

Table 1. Classification of β-Ti based on Mo_{eq} values [5]

Type of Ti	Mo_{eq} value
β-rich Ti	0~5
Near β-Ti	5~10
Metastable β-Ti	10~30
Stable β-Ti	> 30

and precision forming operations [6]. β-stabilizers are typically categorized into isomorphous elements (e.g., Mo, Nb, V), which are fully soluble in Ti, and eutectoid elements (e.g., Fe, Co), which exhibit partial solubility [5, 7]. Specifically, Fe, being an eutectoid element, is more abundant in the Earth's crust compared to isomorphous elements, rendering it a cost-effective choice. Additionally, Fe contributes to solid solution strengthening, which has led to extensive research into the incorporation of Fe into Ti alloys to develop low-cost β-Ti alloys [8–13].

Meanwhile, Ti and its alloys present significant machining challenges at room temperature. Their low machinability hinders the production of intricate shapes required by advanced industries when using conventional methods such as casting or forging. Several studies have explored the use of additive manufacturing (AM) technologies, employing metal powders, to overcome these limitations in Ti alloy production [14-16]. One such method is laser powder bed fusion (L-PBF), which involves the selective irradiation of a laser onto thin layers of metal powder, each approximately 30 μm in thickness, to construct three-dimensional structures. Among various additive manufacturing techniques, L-PBF offers superior dimensional accuracy and high design flexibility, making it particularly suitable for fabricating complex Ti alloy geometries. In the production of β-Ti alloys via the L-PBF process, it is essential to use pre-alloyed spherical powders containing β phase stabilizing elements as alloying constituents to ensure a smooth process. However, the production of pre-alloyed powders is generally costly and, depending on the composition ratio, can be difficult to achieve, which often results in the inability to produce powders with specific compositions.

Therefore, in this study, β-Ti alloys were fabricated using an in-situ alloying process applied to non-spherical pure Ti powder, which was individually mixed with β phase stabilizing elements, rather than utilizing pre-alloyed powders, to facilitate alloying during the L-PBF process. This approach not only allows for the precise design of alloys with the desired composition ratios but also ensures cost-effectiveness, as the powders are not subjected to alloying or spheroidization processes and are mixed separately [17]. Indeed, studies utilizing the advantages of the L-PBF based in-situ alloying process for alloy design and production have been documented. For example, a Ti-34Nb alloy was successfully produced using the in-situ alloying technique with Ti and niobium (Nb) powders, where the challenges of porosity and unmelted particles were addressed by adjusting process parameters [18]. Similarly, another study demonstrated the potential of producing functional composites with hardness gradients by utilizing Ti and Mo powders in the in-situ alloying process, facilitated by layer-by-layer energy control [19]. Research has also been conducted to examine process variables and mechanical properties during manufacturing, not solely focused on alloy design. However, when using elemental powders with varying melting points and densities, these powders can melt and diffuse during processing, leading to alloying and potentially causing local concentration gradients or microstructural inhomogeneities, depending on the process conditions [20]. To ensure successful in-situ alloying, it is crucial to optimize L-PBF process parameters, such as laser power and scan speed, and to analyze the relative density and microstructure of the resulting specimens.

In this study, the Fe content was set at 3 wt.% to produce a near β-Ti alloy that stabilizes the β phase while allowing the coexistence of the α phase. The mixed powder used in the in-situ alloying process was prepared by incorporating 0.1 wt.% SiO_2 hydrophobically treated oxide nanoparticles to improve the flowability of the non-spherical pure Ti powder. In a previous study, our research team confirmed the enhancement of flowability and oxide-based strength through the dry coating of SiO_2 nanoparticles with non-spherical hydrogenation-dehydrogenation (HDH) Ti-6Al-4V powder [21]. We employed the same technique to prepare the mixed powder for this study. Optimal process conditions were determined by combining 25 process variables within the volumetric energy density (VED) range of 31.75-214.30 J/mm^3, ensuring that specimens with a relative density of 99 % or higher were produced. Additionally, pure Ti specimens were fabricated under the same conditions and used as a control group to assess differences in microstructure and mechanical properties based on the alloy composition. The phase composition and elemental distribution of the fabricated specimens were analyzed using X-ray diffraction (XRD) and energy dispersive spectroscopy (EDS), and the microstructure of the layered specimens was examined using optical microscopy (OM) and scanning electron microscopy (SEM). Vickers hardness measurements and tensile tests were conducted to evaluate the mechanical properties and confirm changes resulting from the addition of Fe.

2. Experimental

In this experiment, non-spherical pure Ti powder (<45 μm, Samhwa Steel), spherical Fe powder (40-50 μm, Avention), and hydrophobic surface-treated SiO_2 nanoparticles (5-15 nm, Skyspring Nanomaterials) were used. To assess the size and distribution of the base Ti and alloying element Fe powders, particle size analysis (PSA; Particle Size Analysis, Shympatec, HELOS QUIXEL) was conducted. To improve the flowability of the non-spherical pure Ti powder, SiO_2 nanoparticles were dry-coated at a 0.1 wt.% ratio using a turbula mixer at 3000 rpm for 3 hours. Fe powder was then mixed with the SiO_2-treated Ti powder at a 3 wt.% ratio under the same conditions.

To evaluate the flow characteristics of the mixed powder and its suitability for the PBF process, Hall flowmeter measurements were conducted, and apparent density and tap density were measured using a tap densimeter. The time it took for 50 g of powder to fall through a standard funnel with a 25 mm diameter orifice was measured five times, and the average time was used for Hall flowmeter analysis. For a quantitative evaluation of flow characteristics, the Hausner ratio, calculated as the ratio of apparent density to tap density, was derived and compared.

The mixed powder was used to fabricate specimens with dimensions of 10 × 10 × 5 mm using an L-PBF machine (AnyX-120, CSCAM). The additive manufacturing process was carried out in a high-purity argon atmosphere, with recoating speed, layer thickness, and hatch spacing fixed at 30 mm/s, 0.03 mm, and 0.14 mm, respectively. Laser power and scan speed were set as process variables, resulting in the fabrication of 25 specimens with different laser powers and scan speeds.

For phase analysis of the fabricated specimens, X-ray diffraction (XRD; D8 ADVANCE, Bruker) was performed within a 20-90° diffraction angle range at 3 °/min, and elemental distribution was analyzed using energy dispersive spectroscopy (EDS; ZEISS, Gemini360). Microstructural analysis was carried out using scanning electron microscopy (SEM; ZEISS, LEO “SUPRA 55”), and optical microscopy (OM; ZEISS, Axioscope 5).

To compare the mechanical properties before and after alloying, Vickers hardness measurements were performed with a 500 gf load and 10-second dwell time for 10 cycles, and the average value was calculated. Tensile tests were conducted using ASTM E8 specimens (Fig. 1) produced under the same conditions, and the average value was derived after three measurements using a tensile testing machine (SHIMADZU CORPORATION, AG-Retrofit).

3. Results and Discussion

3.1 Powder preparation

The morphologies of the Ti and Fe powder used in this study are shown in the SEM images in Fig. 2(a) and (b). Fig. 2 (a) particles produced via HDH process exhibit a non-spherical morphology, whereas (b) particles produced by gas atomization feature a rounded, spherical shape. Fig. 2(c) presents the particle size analysis results, indicating that the d50 of Ti is 32.19 μm and that of Fe is 42.66 μm. Given that the size difference between the Ti base material and the Fe alloy element powder is several μm, powders with a relatively small particle size difference were selected to ensure the stability of the mixed powder and the process. No Fe peaks were detected in the X-ray diffraction (XRD) pattern after powder mixing (Fig. 2(d)), which can be attributed to the low Fe content of 3 wt.%.

The results of the flowability evaluation, which confirm the applicability of the L-PBF process to the mixed powder, are presented in Table 2. A previous study conducted by our research team [21] demonstrated that the addition of 0.1 wt.% SiO_2 nanoparticles to non-spherical Ti-6Al-4V powder significantly improved its flow characteristics, making it suitable for the L-PBF process. Therefore, a similar evaluation of the flowability of Ti-3Fe powder, both before and after dry coating with 0.1 wt.% SiO_2 nanoparticles, was performed. The Ti-3Fe powder mixture without SiO_2 addition exhibited extremely poor flow properties, making measurement with a Hall flowmeter unfeasible. In contrast, the Ti-3Fe + 0.1 wt.% SiO_2 powder mixture showed flow properties comparable to those reported in

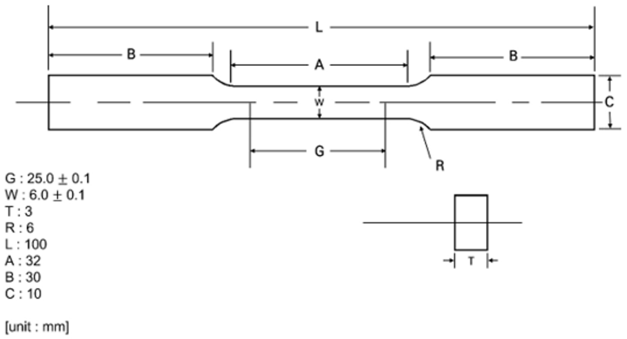

Fig. 1. Schematic of the tensile specimen according to ASTM E8 standards

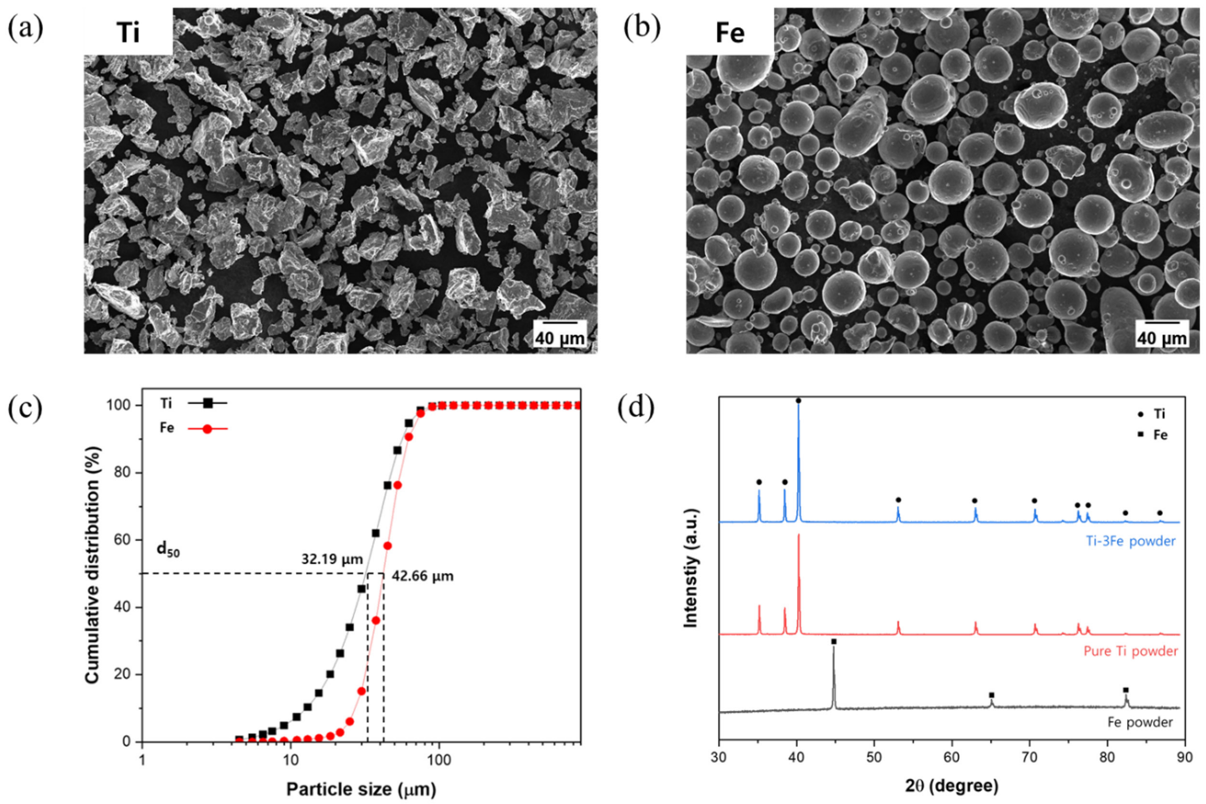

Fig. 2. (a), (b) Scanning electron microscopy image of Ti and Fe powder, (c) particle size analysis results of the powder, (d) X-ray diffraction patterns before and after mixing of the powders

Table 2. Flow characteristics of Ti-3Fe mixed powder before and after the addition of SiO_2

	Ti-3Fe	Ti-3Fe + 0.1 wt.% SiO_2
Hall flowmeter (Standard, s/50 g)	No flow	92.61 ± 3.14
Hall flowmeter (Carney, s/50 g)	No flow	16.75 ± 0.94
Hausner ratio	1.40	1.15

previous studies. Specifically, the Hausner ratio, which is calculated by dividing the apparent density by the tap density, indicates excellent flowability when it approaches 1 [22]. The mixed powder with SiO_2 addition exhibited even better flow properties, with a value of 1.15 – approximately 0.05 lower than the values reported in previous studies. The flow property evaluation results when SiO_2 nanoparticles were added to Ti-3Fe powder were comparable to, or in some cases superior to, those observed in previous studies that successfully achieved layering. Therefore, we conclude that there should be no issues in applying the L-PBF process to this material.

3.2 L-PBF process and sample fabrication

Even when the same material is used, characteristics such as microstructure and relative density can vary depending on the process conditions for specimens produced by the L-PBF process. This variation arises because the morphology and geometric structure of the melt pool formed during the process are influenced by the process variables. Therefore, it is essential to determine the optimal combination of the four key L-PBF process variables: laser power (P), scan speed (v), hatch spacing (h), and layer thickness (t). The volumetric energy density (VED), calculated using equation (2), serves as a quantitative thermodynamic indicator and is primarily used to optimize the L-PBF process [23].

$$\mathrm{VED} = \frac{\mathrm{P}}{\mathrm{v} \cdot \mathrm{h} \cdot \mathrm{t}} \tag{2}$$

In this study, the process conditions were optimized by fixing the layer thickness and hatch spacing, while laser power and scan speed – the variables related to the laser irradiation – were selected as the primary variables. A total of 25 process conditions, involving different laser power and scan speed settings within the VED range of 31.75-214.30 J/mm^3, were combined to produce the specimens shown in Table 3.

As mentioned above, VED is a thermodynamic quantitative indicator, meaning it quantifies the amount of energy injected per unit volume. However, it does not account for the geometric behavior determined by the depth of the molten pool formed during the process, nor its internal dynamics [24]. For example, even when two specimens yield the same VED value with different combinations of process variables, their microstructures and mechanical properties may vary depending on the specific variables employed. Therefore, in this study, VED was not used as an absolute indicator for process optimization, but rather as a comparative value between different process conditions. Optimization was performed based on the relative density and microstructure analysis of the produced samples.

3.3 Phase and microstructure analysis

XRD pattern analysis of the produced specimens (Fig. 3) revealed that the α'-Ti peak was dominant overall, although some β-Ti peaks remained at room temperature. This is due to the transformation of the β phase into α' martensite caused by the rapid cooling during the L-PBF process. As no peaks corresponding to the α-Fe phase or the intermetallic compounds TiFe or $TiFe_2$ were observed, it can be inferred that Fe exists in a dissolved state within the Ti lattice rather than as a separate phase. Furthermore, when comparing the XRD patterns of pure Ti specimens produced under the same conditions, it was observed that the α'-Ti peak of Ti-3Fe shifted slightly towards the high-angle region (increased 2θ). Peak shifts to the low- or high-angle regions can result from various factors, but in this study, we focused on the changes in the Ti lattice caused by the addition of Fe to interpret this phenomenon.

The atomic radii of Ti and Fe are generally known to be 147 pm and 126 pm, respectively [25]. According to the Hume-Rothery rule [26], two atoms can form a solid solution through substitution when the difference in their radii is within 15 %. Ti

Table 3. L-PBF process conditions and resulting volumetric energy density (VED)

Sample number	Laser power (W)	Scan speed (mm/s)	Hatch spacing (mm)	Layer thickness (mm)	VED (J/mm^3)	Relative density (%)
1	80	600	0.14	0.03	31.75	93.66
2	80	500	0.14	0.03	38.10	94.63
3	80	400	0.14	0.03	47.62	95.08
4	80	300	0.14	0.03	63.49	96.20
5	80	200	0.14	0.03	95.24	96.96
6	100	600	0.14	0.03	39.68	97.48
7	100	500	0.14	0.03	47.62	97.57
8	100	400	0.14	0.03	59.52	96.47
9	100	300	0.14	0.03	79.37	95.73
10	100	200	0.14	0.03	119.05	97.90
11	120	600	0.14	0.03	47.62	98.68
12	120	500	0.14	0.03	57.14	98.91
13	120	400	0.14	0.03	71.43	97.12
14	120	300	0.14	0.03	95.24	96.31
15	120	200	0.14	0.03	142.86	97.98
16	150	600	0.14	0.03	59.52	98.52
17	150	500	0.14	0.03	71.43	99.12
18	150	400	0.14	0.03	89.29	99.21
19	150	300	0.14	0.03	119.05	98.83
20	150	200	0.14	0.03	178.57	99.01
21	180	600	0.14	0.03	71.43	99.07
22	180	500	0.14	0.03	85.71	98.63
23	180	400	0.14	0.03	107.14	98.62
24	180	300	0.14	0.03	142.87	98.92
25	180	200	0.14	0.03	214.30	98.56

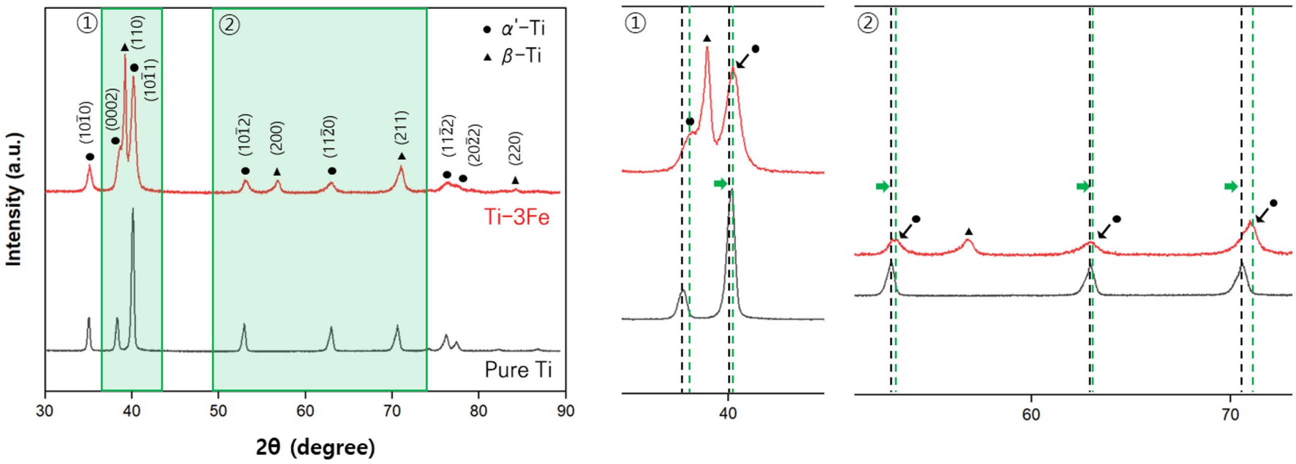

Fig. 3. X-ray diffraction patterns of Ti-3Fe and pure Ti fabricated specimens, and enlarged regions ① and ② for peak shift analysis

and Fe have a radius difference of approximately 14.29 %, which means they fall within the range where solid solution formation is feasible during alloying. Therefore, when the relatively smaller-radius element Fe is dissolved into the Ti matrix, lattice contraction occurs in the solid solution, resulting in distortion and a decrease in interplanar spacing and lattice constants [27]. The interplanar spacing (d) was calculated using peak angle (2θ) of the (0002) and (101¯0) planes of α'-Ti (in Fig. 3) by plugging it into Bragg's law (3). The derived interplanar spacing was then used to calculate the lattice constants (a, c) of the α-Ti HCP structure using equation (4), thereby confirming the change in lattice constants [28].

$$n\lambda = 2dsin\theta \tag{3}$$

$$\frac{1}{\mathrm{d}_{\mathrm{hkl}}^{2}} = \frac{4}{3} \cdot \frac{\mathrm{h}^{2} + \mathrm{hk} + \mathrm{k}^{2}}{\mathrm{a}^{2}} + \frac{1^{2}}{\mathrm{c}^{2}} \tag{4}$$

The calculation results are presented in Table 4. The theoretical calculations, based on the peak angle, reveal that the lattice constants a and c of Ti-3Fe decreased by 0.14 % and 0.51 %, respectively, compared to pure Ti with no Fe added. This indicates that the reduction in interplanar spacing and lattice constants, caused by the addition of Fe, resulted in a shift of the XRD peaks towards the high-angle region. This suggests that the Fe elements added during the powder mixing stage formed a solid solution with Ti.

Table 4. Interplanar spacing (d), lattice constants (a, c), and calculation results

	Pure Ti	Ti-3Fe
d_{100} (Å)	2.559 (2θ = 35.09°)	2.557 (2θ = 35.11°)
d_{002} (Å)	2.341 (2θ = 38.40°)	2.329 (2θ = 38.65°)
a (Å)	2.957	2.953
c (Å)	4.682	4.658

The results of the relative density measurements according to the VED of 25 specimens are shown in Fig. 4(a). While there was a general trend of increasing relative density with higher VED values, no specific correlation, such as a linear proportional relationship, was observed. However, specimens within the 70-90 J/mm^3 range exhibited relatively high relative densities. Specimen #18, with a VED value of 89.29 J/mm^3, had the highest relative density at 99.21 %. EDS mapping of specimen #18 in Fig. 4(b) reveals that the added Fe is uniformly distributed throughout the Ti matrix. Accordingly, specimen #18 was designated as the optimal condition, and all subsequent analyses were performed on specimens fabricated under that setting.

Fig. 5 show OM and SEM images of Ti-3Fe and pure Ti specimens fabricated under the same conditions in their as-built state. As shown in Fig. 5(a) and (b), both types of specimens formed a non-equilibrium lamellar α' martensite phase due to the rapid melting and cooling that occurs during the L-PBF process. The same microstructure is observed in the SEM images in Fig. 5(c) and (d), which is typical of specimens produced by L-PBF. Ti alloys containing 3 wt.% Fe exhibit the same α' martensite-dominated microstructure as pure Ti specimens, as they correspond to near β-Ti alloys and undergo no phase transformation. When approximately 9 wt.% or more of Fe is added, dendritic-shaped TiFe or TiFe$_2$ precipitates are typ-

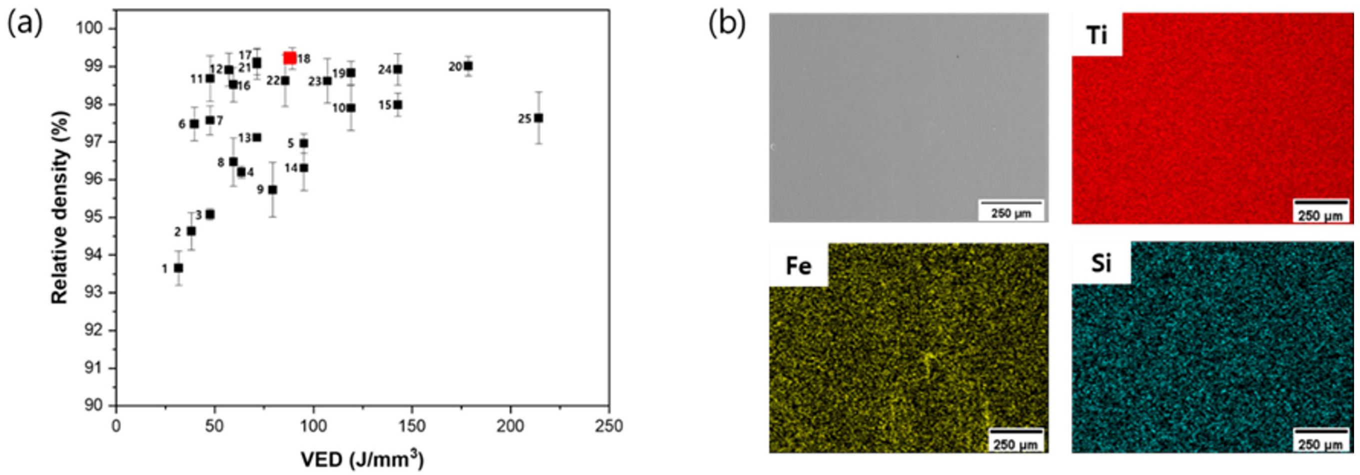

Fig. 4. (a) Relative density measurements as a function of volumetric energy density (VED), (b) energy dispersive spectroscopy mapping of specimen #18

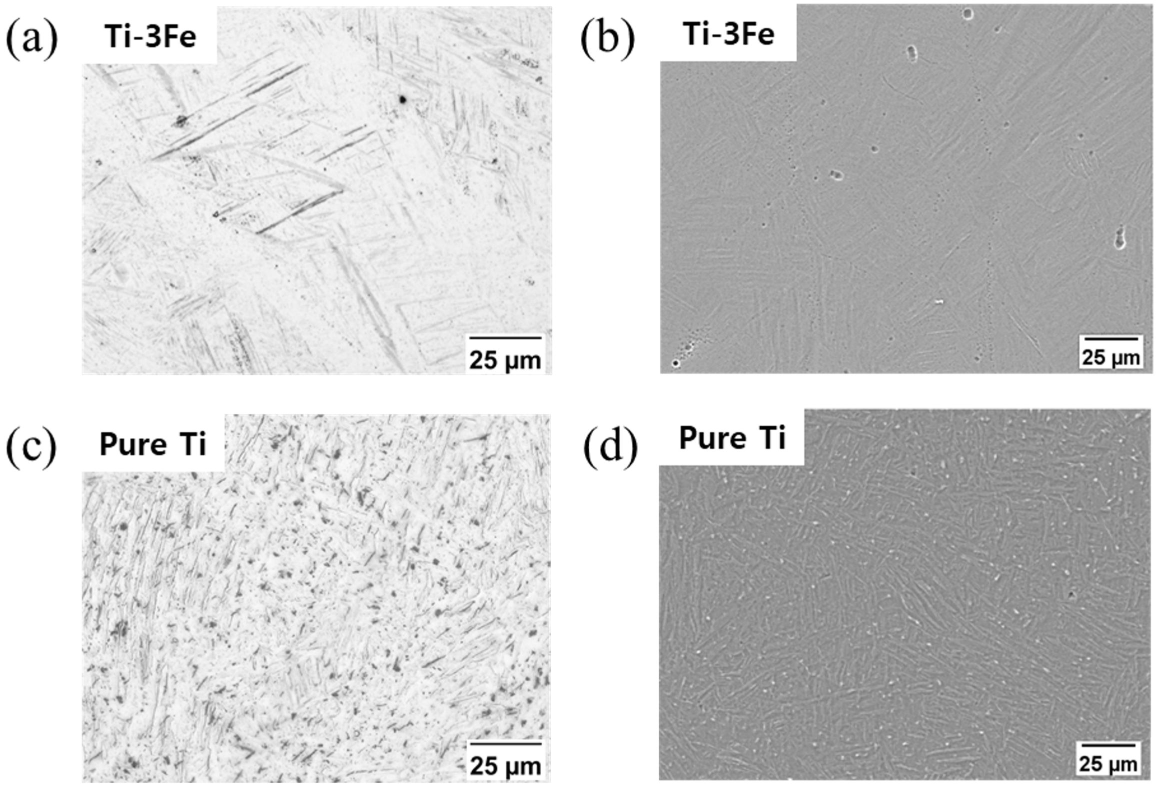

Fig. 5. (a), (c) Optical microscopy images of pure Ti and Ti-3Fe as-built specimens, (b), (d) scanning electron microscopy images of pure Ti and Ti-3Fe as-built specimens

ically observed [29]. However, such intermetallic compounds were not observed in this study due to the low Fe content.

3.4 Mechanical properties

Fig. 6 shows a graph comparing the Vickers hardness of 25 Ti-3Fe specimens with that of 25 pure Ti specimens, both of which were under the same process conditions. The average values obtained from 10 measurements are presented in Table 5. The hardness values for the Ti-3Fe and pure Ti specimens were 470.80 HV and 315.56 HV, respectively, showing an improvement in hardness of Ti-3Fe alloy approximately 49.19 % compared to pure Ti. This enhancement is attributed not only to the solid solution strengthening effect caused by the incorporation of Fe into Ti lattice (as confirmed in Section 3.3), but also to oxide dispersion strengthening resulting from the addition of SiO_2 nanoparticles to improve flowability. Two strengthening pathways are distinguished. Fe (composition-driven) acts as a β-stabilizer and dissolves in the Ti matrix; the absence of Fe or Ti-Fe intermetallic reflections together with high-angle XRD peak shifts (lattice contraction) evidences solid-solution formation. This composition change provides a direct contribution to the observed increases in strength/hardness and aligns with the work hardening behavior in some stress-strain curves. SiO_2 (microstructure-driven) promotes martensite grain size reduction under the L-PBF process (pinning-assisted refinement). In our research team's previous study [21], SiO_2 treatment of Ti-based powders produced an ~36.8 % decrease in martensite grain size verified by EBSD IPF maps, accompanied by higher hardness/strength, supporting a grain-refinement-mediated contribution relevant here. Because dispersion-related effects were not quantitatively isolated in the present dataset, we do not assign a numerical partition between the Fe and SiO_2 contributions. This limitation is deemed addressable by targeted nanoscale characterization-e.g., high-resolution TEM/STEM-EDS (and, where appropriate, APT or synchrotron XRD)-which is expected to enable quantitative resolution of dispersion-related contributions.

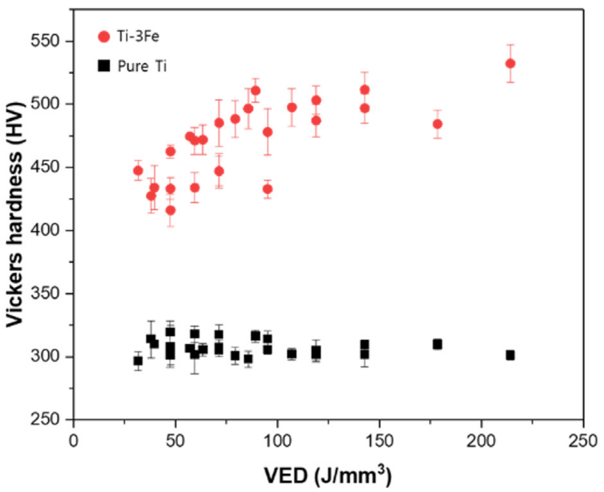

Fig. 6. VED-Vickers hardness graph of Ti-3Fe and pure Ti specimens

Table 5. Comparison of average Vickers hardness values for specimen #18 Ti-3Fe and specimen #18 pure Ti

Specimen	Vickers hardness (HV)
Ti-3Fe	470.80 ± 29.34
Pure Ti	315.56 ± 4.65

The Ti-3Fe alloy exhibits superior strength compared to pure Ti due to the solid solution strengthening effect and the oxide dispersion strengthening effect induced by the addition of SiO_2 nanoparticles, both of which were discussed in the previous section. As shown in Fig. 7 and Table 6, which present the stress-strain curve and tensile properties derived from actual tensile tests, the yield and ultimate tensile strengths of the Ti-3Fe alloy increased by 44.6 % and 52.3 %, respectively, compared to pure Ti. However, the elongation of the Ti-3Fe alloy is slightly lower than that of pure Ti, which can be attributed to lattice distortion caused by addition of Fe, as observed previously. While the addition of Fe enhances strength through solid solution strengthening, it also induces brittle behavior due to stress concentration caused by lattice distortion [30, 31]. In summary, the addition of Fe improves yield strength, tensile strength, and hardness through solid solution strengthening and the oxide dispersion strengthening effect of the added SiO_2 nanoparticles. However, lattice distortion leads to embrittlement, resulting in a decrease in elongation.

Meanwhile, in the stress-strain curve shown in Fig. 7, pure Ti exhibits a nearly horizontal curve with little increase in stress until fracture occurs after yield, shows a tendency for stress to increase even after the yield point. This behavior is typical characteristic of work hardening, which results from delayed necking due to the continuous accumulation of dislocations within the Ti-3Fe alloy during plastic deformation. Work hardening refers to the phenomenon where the strength of a material increases as the degree of deformation increases during plastic deformation. Accordingly, in this study we interpret the work hardening as arising from two indirect effects associated with Fe addition. First, Fe addition primarily elevates the initial yield strength via solid-solution strengthening, while also giving rise to lattice distortion and solute-induced stress fields that can impede dislocation motion and retard dynamic recovery. As Fe is solubilized into the Ti lattice, as previously described, lattice distortion and a stress field arise due to differences in atomic radii, which induce the solid solution strengthening effect [32]. The stress field generated at this stage acts as additional resistance during dislocation movement, delaying their rearrangement and annihilation. As a re-

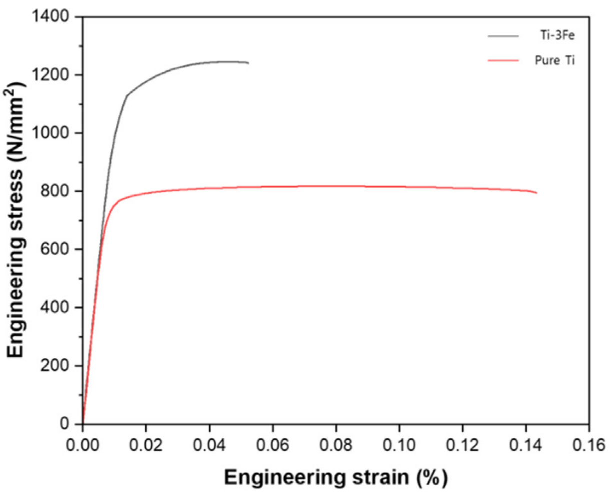

Fig. 7. Stress-strain curve of Ti-3Fe and pure Ti specimens

Table 6. Tensile test results for each specimen: yield strength, ultimate tensile strength, and elongation

Properties	Ti-3Fe	Pure Ti
Yield strength (MPa)	1063.85 ± 50.63	735.73 ± 2.16
Ultimate tensile strength (MPa)	1245.45 ± 44.86	817.66 ± 8.83
Elongation (%)	5.22 ± 0.26	14.33 ± 1.10

sult, the dislocation density retention time increases, and stress continues to accumulate, serving as a mechanism that promotes work hardening. Second, based on reports that solute alloying in Ti alloys reduces the stacking-fault energy (SFE) [33], Fe addition likewise leads to an approximately linear decrease in SFE; since lower SFE generally increases strain hardening [34], we regard this as an additional indirect effect of Fe addition. Therefore, in the elongation region of Fig. 7, the Ti-3Fe alloy shows a post-yield rise in stress indicative of work hardening, confirming that Fe addition not only induces solid-solution strengthening but also contributes to work hardening. In contrast, the pure Ti specimen exhibits an essentially flat post-yield segment, and no discernible work hardening was observed for pure Ti under our test conditions.

4. Conclusion

In this study, near β-Ti was produced by adding 3 wt.% of Fe powder, a eutectoid β-stabilizer, and 0.1 wt.% of SiO_2 nanoparticles to improve flowability to pure Ti powder, and then inducing alloying during the process using an in-situ alloying method. To compare the microstructure and mechanical properties before and after Fe addition, pure Ti specimens were used as a control group for comparative analysis.

- Based on two process conditions (laser power and scan speed) of L-PBF, 25 specimens with different process conditions were produced, and the process conditions were optimized for specimens with a relative density of 99 % or higher. To analyze the effect of the alloying element Fe, pure Ti specimens were produced under the same optimized process conditions, and their microstructure and mechanical properties were compared and analyzed.
- XRD pattern analysis confirmed the presence of the β phase at room temperature and the peak shift phenomenon in the high-angle region. In this study, we interpreted this phenomenon by focusing on the decrease in interplanar spacing and lattice constants due to dissolved Fe in the Ti matrix. The lattice constants a and c of the actual HCP structure were calculated to have decreased by 0.14 % and 0.51 %, respectively, using equations (3) and (4). Additionally, EDS mapping confirmed that Fe was uniformly dissolved throughout the specimen.
- When comparing the mechanical properties of pure Ti specimens and Ti-3Fe specimens, the hardness of Ti-3Fe specimens improved by approximately 49.19% compared to pure Ti specimens, and the yield strength and ultimate tensile strength increased by 44.6 % and 52.3 %, respectively. However, the elongation of the Ti-3Fe specimen showed a slight decrease compared to the pure Ti specimen, which was attributed to brittleness induced by internal stress concentration resulting from lattice distortion.

Funding

This work was supported by the National Research Foundation of Korea (NRF) grant funded by the Korean government (Grant No. RS-2023-00212081) and by Korea Institute of Energy Technology Evaluation and Planning (KETEP) grant funded by the Korean government (MOTIE)(RS-2024-00349003), Support for on-site practical training linked to public enterprises).

Conflict of Interest

B. Lee serves as an editor of the Journal of Powder Materials editing, but has no role in the decision to publish this article. Except for that, no potential conflict of interest relevant to this article was reported.

Data Availability Statement

Data will be made available on request.

Author Information and Contribution

Sehun Kim: MSc student; Conceptualization of the study, original manuscript drafting.

Ukju Gim: MSc student; Preparation and surface treatment of Ti powder; SiO_2 nanoparticle coating.

Taehu Kang: MSc student; L-PBF process trials under varied energy densities, Review & Editing.

Jongik Lee: MSc student; Microstructural characterization by OM, XRD, Review & Editing.

Sanghee Jeong: MSc student; SEM imaging, Review & Editing.

Jimin Han: Undergraduate student; Review & Editing.

Bin Lee: Associate professor; Project supervision and funding acquisition, overall study conceptualization, critical review and editing of the manuscript; correspondence with the journal.

Acknowledgments

None.

ORCID

Bin Lee, https://orcid.org/0000-0002-9906-9651

References

[1] P. Pushp, S. M. Dasharath and C. Arati: Mater. Today Proc., **54** (2022) 537.

[2] J. C. Williams and R. R. Boyer: Metals(Basel), **10** (2020) 705.

[3] C. Veiga, J. P. Davim and A. J. R. Loureiro: Rev. Adv. Mater. Sci., **32** (2012) 133.

[4] J. D. Cotton, R. D. Briggs, R. R. Boyer, S. Tamirisakandala, P. Russo, N. Shchetnikov and J. C. Fanning: JOM, **67** (2015) 1281.

[5] R. P. Kolli and A. Devaraj: Metals, **8** (2018) 506.

[6] P. Pesode and S. Barve: J. Eng. Appl. Sci., **70** (2023) 25.

[7] F. Huber, T. Papke, C. Kauffmann, R. Rothfelder, P. Krakhmalev, M. Merklein and M. Schmidt: Mat. Sci. Eng., **A, 808** (2021) 141374.

[8] S. G Careau, E. Ulate-Kolitsky and B. Tougas: Mater., **24** (2022) 101471.

[9] W. Wang, X. Zhang and J. Sun: Mat. Charact., **142** (2018) 398.

[10] S. Ma, X. Min, M. Lv and J. Dai: Mater. Sci. Eng., **A, 898** (2024) 146372.

[11] G. Al-Makhzumi, K. L. Dahm, F. Yang and L. Bolzoni: Mater. Chem. Phys., **308** (2023) 128244.

[12] H. Wang, H. L. Luo, J. Q. Chen, J. C. Tang, X. Y. Yao, Y. H. Zhou and M. Yan: Mat. Character., **182** (2021) 111526.

[13] H. Hwang, Y. Lee, J. Park and D.-G. Lee: J. Powder Mater., **29** (2022) 325.

[14] C. Ni, J. Zhu, B. Zhang, K. An, Y. Wang, D. Liu, W. Lu, L. Zhu and C. Liu: Virt. Phys. Prototy., **20** (2025) e2446952.

[15] S. Cao, Y. Zou, C. V. S. Lim and X. Wu: Light: Adv. Manuf., **2** (2021) 20.

[16] J. C. Colombo-Pulgarín, C. A. Biffi, M. Vedani, D. Celentano, A. Sánchez-Egea, A. D. Boccardo and J.-P. Ponthot: J. Mater. Eng. Perform., **30** (2021) 6365.

[17] M. S. Knieps, W. J. Reynolds, J. Dejaune, A. T. Clare and A. Evirgen: Mater. Sci. Eng., **A, 807** (2021) 140849.

[18] S. Huang, R. L. Narayan, J. H. K. Tan, S. L. Sing and W. Y. Yeong: Acta Mater., **204** (2021) 116522.

[19] R. Duan, S. Li, B. Cai, Z. Tao, W. Zhu, F. Ren and M. M. Attallah: Composites, Part B, **222** (2021) 109059.

[20] S. Wei, Y. Zhao, B. Zhang, P. Wang and U. Ramamurty: Mat. Sci. Eng. A, **888** (2023) 145795.

[21] U. Gim, S. Kim, T. H. Kang, J. Lee, S. Jeong, J. Han and B. Lee: Powder Metall., **68** (2025) 95.

[22] B. Lee, D.-K. Kim, Y. I. Kim, D. H. Kim, Y. Son, K.-T. Park and T.-S. Kim: J. Powder Mater., **27** (2020) 509.

[23] R. Zhao, C. Chen, W. Wang, T. Cao, S. Shuai, S. Xu, T. Hu, H. Liao, J. Wang and Z. Ren: Addit. Manuf., **51** (2022) 102605.

[24] U. Scipioni Bertoli, A. J. Wolfer, M. J. Matthews, J. P. R. Delplanque and J. M. Schoenung: Mater. Des., **113** (2017) 331.

[25] N. N. Greenwood, N. Neill and A. Earnshaw, Chemistry of the Elements, 2nd edElsevier, (2012).

[26] Q. F. He, Y. F. Ye and Y. Yang: J. Phase Equilib. Diffus., **38** (2017) 416.

[27] A. Kilmametov, Y. Ivanisenko, B. Straumal, A. A. Mazilkin, A. S. Gornakova, M. J. Kriegel, O.B. Fabrichnaya, D. Rafaja and H. Hahn: Scr. Mater., **136** (2017) 46.

[28] Z. Elahi and W. Gull: Spreadsheets in Eudcation. Indexing the X-Ray Diffraction Patterns of Cubic and Hexagonal Structures Using Spreadsheets, (2024).

[29] T. Teramae, T. Tanaka, M. Fukuo, K. Shitata, J. Umeda, S. Li, A. Alhazaa and K. Kondoh: J. Alloys Compd., **858** (2021) 158292.

[30] M. A. Haq, I. Ali, Y. Song and B. S. Kim: Mater. Today Commun., **38** (2024) 107743.

[31] Z. He, W. Yang, C. Liu, X. Wei and J. Wang: Metals(Basel), **14** (2024) 198.

[32] H. M. Kim, Y. J. Lee, J. G. Lee and D. G. Lee: J. Mater. Res. Technol., **33** (2024) 7406.

[33] A. Yu: SCIREA J. Phys., **1** (2016) 1.

[34] D. T. Pierce, J. A. Jiménez, J. Bentley, D. Raabe and J. E. Wittig: Acta Mater., **100** (2015) 178.